Differential characterization of lumbar spine associated tissue histology with nonlinear optical microscopy

FEI ZOU,[1,7] LILI ZHANG,[2,3,7] XIANG ZOU,[4,7] JING HUANG,[2] CONG NIE,[1] JIANYUAN JIANG,[1] CHONGYUAN GUO,[5] HONGLI WANG,[1,8] XIAOSHENG MA,[1,9] AND MINBIAO JI[2,6,10] (iD)

[1] *Department of Orthopaedics, Huashan Hospital, Fudan University, Shanghai 200040, China*
[2] *State Key Laboratory of Surface Physics and Department of Physics, Human Phenome Institute, Multiscale Research Institute of Complex Systems, Academy for Engineering and Technology, Key Laboratory of Micro and Nano Photonic Structures (Ministry of Education), Fudan University, Shanghai 200433, China*
[3] *State Key Laboratory of Infrared Physics, Shanghai Institute of Technical Physics, Chinese Academy of Sciences, Shanghai 200083, China*
[4] *Department of Neurosurgery, Huashan Hospital, Fudan University, Shanghai 200040, China*
[5] *Shanghai Starriver Bilingual School, Shanghai 201108, China*
[6] *Yiwu Research Institute of Fudan University, Chengbei Road, Yiwu City, Zhejiang 322000, China*
[7] *These authors contributed equally.*
[8] *wanghongli@huashan.org.cn*
[9] *dr_maxiaosheng@126.com*
[10] *minbiaoj@fudan.edu.cn*

Abstract: Percutaneous endoscopic lumbar discectomy (PELD) is the major effective treatment for lumbar disc herniation, and rapid histological identification of dissected tissue is critical to guide the discectomy. In this work, we revealed the histological features of different types of peridural tissues of the lumbar spine by label-free multi-modal nonlinear optical microscopy. Stimulated Raman scattering (SRS) was used to extract lipid and protein distributions, while second harmonic generation (SHG) and two-photon excited fluorescence (TPEF) signals were applied to image the collagen and elastin fibers at the same time. Our results demonstrated that the nonlinear optical features of the dura and adjacent soft tissues were significantly different, showing the potentials of our method for intraoperative differentiation of these critical tissues and improving the surgical outcome of PELD.

1. Introduction

Lumbar disc herniation is a displacement of disc material beyond the area of the intervertebral disc (IVD) space. In Western countries, the prevalence of symptomatic herniated lumbar discs is approximately 1-3%. The highest prevalence is among people aged 30-50, with a male to female ratio of 2:1. This type of disease may cause sciatica and neurological dysfunction. To treat this disease, discectomy has been shown to improve self-reported symptoms and neurological function [1].

Among discectomies, percutaneous endoscopic lumbar discectomy (PELD) has become increasingly popular in recent years, not only because it offers a success rate equal to that of open discectomy but also due to the fact that it offers advantages in terms of back pain, operating time, blood loss, hospital stay and return-to-work time [2–5]. However, doubts remain regarding the feasibility of minimally invasive discectomy because of its small working channel and compromised visualization ability. The small working space makes it difficult to prevent and monitor damage to the dura mater and neural structures [6]. Furthermore, no differences were reported in overall complications, permanent tears or nerve root damage when compared with

open surgery [7]. One critical reason for dura tear and nerve damage is that there is always fibrotic adhesion between the dura and surrounding structures such as herniated discs and ligaments [8,9]. These structures have a similar visual appearance under endoscopy, particularly in patients with large disc herniation (Fig. 1(A), (B) and (C)). As a result, it is very difficult for surgeons to differentiate herniated discs from dura [10].
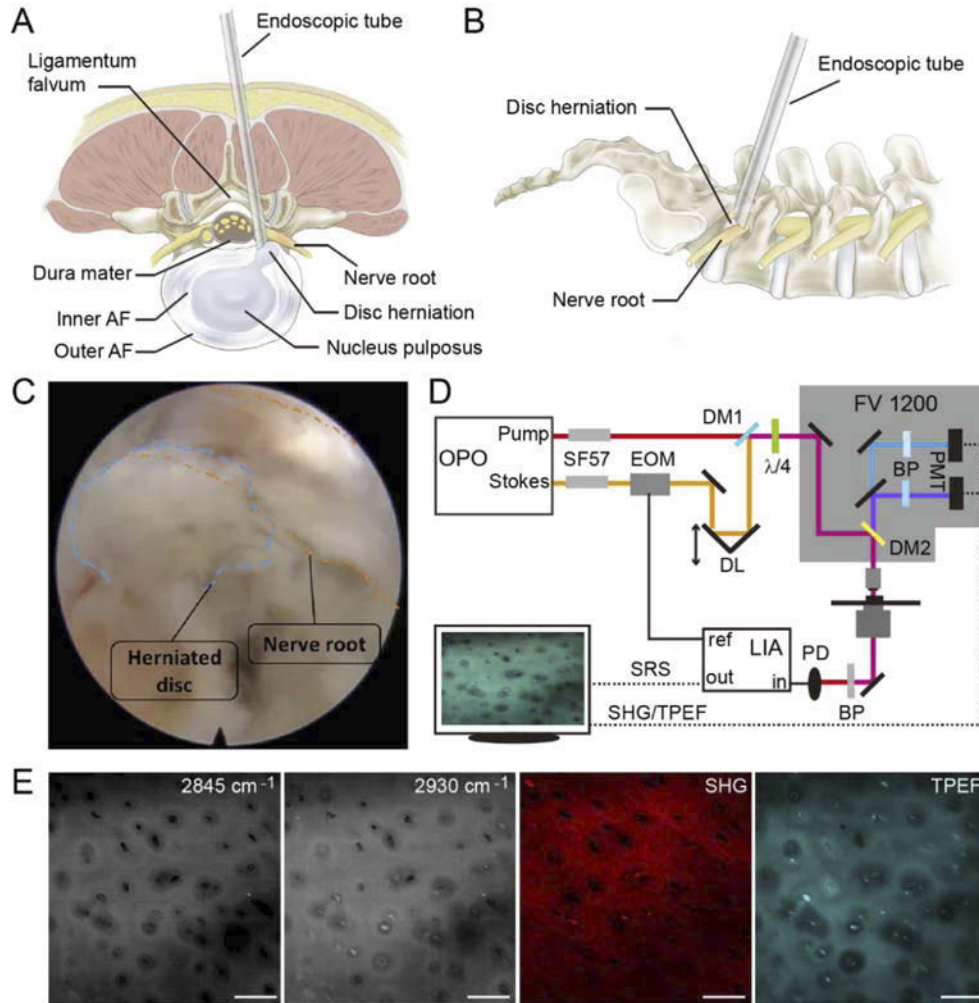

Fig. 1. Experimental design. A. Cross-sectional view of PELD and lumbar spine anatomical illustration. The IVD consists of outer AF, inner AF and nucleus pulposus. B. Lateral view of PELD illustration. C. Endoscopic view of PELD. The borders of the herniated disc (blue dashed line) and nerve root (orange dotted line) are marked. D. Optical layout of the microscope system. E. Multimodal images with SRS, SHG and TPEF of soft tissue. IVD: intervertebral disc; AF: annulus fibrosus; EOM: electro-optical modulator; DL: delay line; DM: dichroic mirror; BP: bandpass filter; $\lambda/4$: quarter-wave plate; PMT: photomultiplier tube; PD: photodiode; LIA: lock-in amplifier. Scale bar: 25 μm.

Although collagen and elastic fibers are present in all peridural structures, the proportions of these fibers differ among the tissues. Based on previous studies, the outer dural border layer consists of fibroblasts with long cell extensions, collagen fibers, and elastic fibers [11]. The nucleus pulposus (NP) inside IVD commonly synthesizes type II collagen, whereas anulus

fibrosus (AF) cells produce both type I and type II collagen [12]. The histology of herniated discs can be very heterogeneous and can include tissues from the NP, AF, or cartilage end plate [13]. With aging, a decrease in elastic fibers and an increase in collagen fibers may be observed in the ligamentum flavum (LF) [14–16], and chondrometaplasia can be found in hypertrophied LF [17].

Currently, studies on lumbar spine-related tissues mainly depend on tissue sectioning and immunohistostaining. To further pave the way for PELD, there is need to investigate label-free imaging methods to distinguish the dura (nerve root) from peridural adhesions under intraoperative setting. Raman spectroscopy has the potential to distinguish different biochemical components in biological tissues based on their fingerprint vibrational spectral identities [18–20], although no or few studies have differentiated peridural structures of the lumbar spine using Raman spectroscopy up to date. On the other hand, traditional spontaneous Raman spectroscopy is very time-consuming for imaging due to the extremely weak scattering efficiency, but by employing stimulated Raman scattering (SRS) microscopy, the imaging speed of biomolecules has been increased up to video-rate, suitable for clinical applications [21–26]. Moreover, second harmonic generation (SHG) and two-photon excited fluorescence (TPEF) are capable of specific detection on collagen and elastic fibers, respectively [27–31].

In this study, we aimed to explore the multi-modal nonlinear optical features of peridural structures of the lumbar spine. Our study firstly revealed the SRS features of lumbar spine structures. In addition, the nonlinear optical responses of the dura and adjacent soft tissues were significantly different, which could be used to effectively differentiate them during PELD. Overall, our results showed the potential to combine nonlinear optical microscopy with PELD for clinical application in the future.

2. Methods

2.1. Sample preparation

Human lumbar IVD, LF and nerve roots were obtained from fresh cadavers, diluted with phosphate-buffered saline (PBS, HyClone) and fixed with 10% paraformaldehyde. After collection, the tissue samples were transferred to the laboratory within 1 hour at -78.5°C on dry ice. The tissue samples were sectioned to a thickness of 10 μm (Ag Protect, Leica) and sealed between two coverslips for further measurements. After nonlinear optical microscopy measurements, the same tissues were stained with hematoxylin and eosin (H&E) for comparison. All tissue collection was approved by the Ethics Committee of Huashan Hospital with informed written consent (KY2019546).

2.2. Microscope system

Our home-built microscope system is illustrated in Fig. 1(D) and could be found in previous work [32]. A pulsed femtosecond (fs) optical parametric oscillator (OPO, Insight DS+, Newport) with dual laser beams was applied as the light source. A fundamental 1040 nm laser beam served as the Stokes beam, while the tunable laser (690-1300 nm) served as the pump beam. To work in the "spectral focusing SRS" mode [33], both laser beams were chirped to several picoseconds (ps) through highly dispersive SF57 glass rods [34–36]. The intensity of the Stokes beam was modulated by an electro-optical modulator (EOM) at 1/4 of the laser pulse repetition rate (20 MHz). The two laser beams were collinearly combined via a dichroic mirror (DMSP1000, Thorlabs). Both beams were circularly polarized to avoid orientational dependence of the fibers [37]. Then, the combined beam was directed into a laser-scanning microscope (FV1200, Olympus) and focused onto the samples with a high NA objective (UPLSAPO 60XWIR, NA 1.2 water, Olympus). The stimulated Raman loss (SRL) signal of the pump beam was transmitted to a bandpass filter (CARS ET890/220, Chroma) and collected by a back-biased photodiode. Finally, the filtered SRL signal was demodulated through a lock-in amplifier (HF2LI, Zurich Instruments)

to generate SRS images. SRS spectra could be acquired by scanning the time delay between pump and Stokes pulses, yielding three-dimensional hyperspectral SRS data in (x, y, and ω), with spectral resolution of ~20 cm^{-1} [24]. The SHG and TPEF signals could be simultaneously detected in epi mode via bandpass filters (FF01-405/10-25, Semrock for SHG; FF01-575/59-25, Semrock for TPEF) and photomultiplier tubes (PMTs). Each field of view (FOV) contained 512×512 pixels with a pixel dwell time of 2 μs. The power levels for the Stokes and pump beams on the samples were approximately 40 mW and 30 mW, respectively. Typical multimodal images of soft tissues are shown in Fig. 1(E).

3. Results

3.1. Differentiating nerve roots with SRS

Typical SRS images and spectra of the nerve root, IVD and LF are shown in Fig. 2, extracted from hyperspectral SRS data [25,32]. These three structures show not only unique morphological appearances in SRS images (Fig. 2(A)), but also distinct spectral features (Fig. 2(B)), indicating different biochemical compositions in these tissues. The nerve roots demonstrated SRS spectral
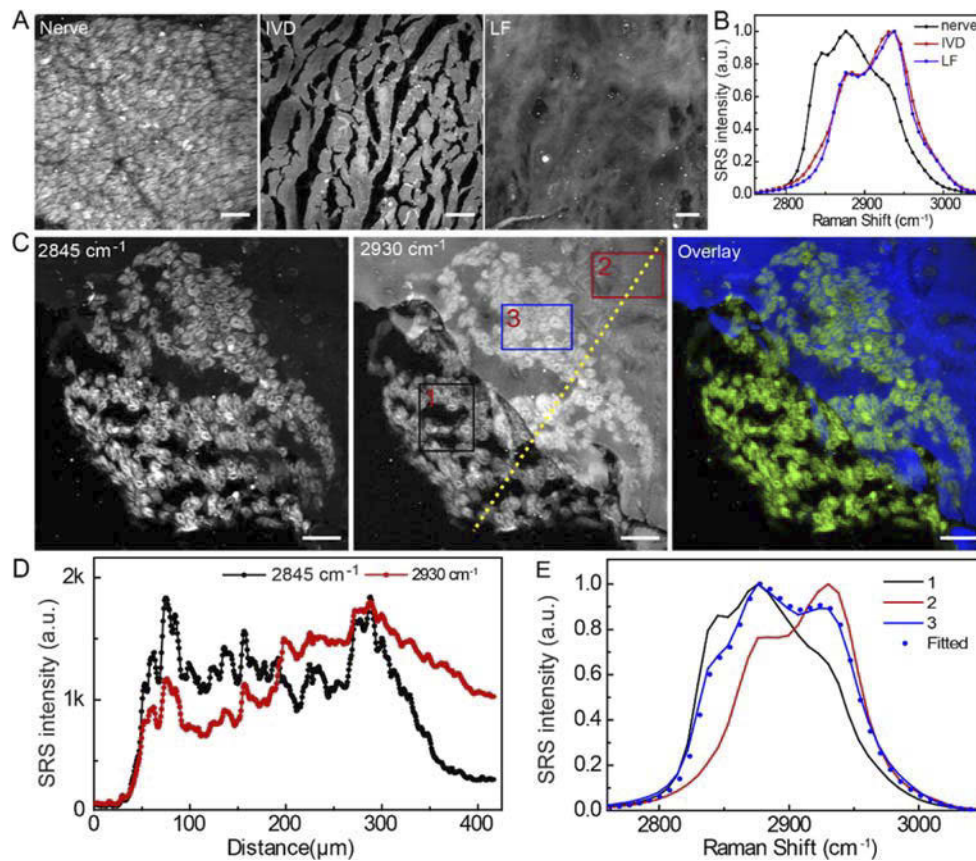

Fig. 2. SRS characterization of the nerve root, IVD and LF. A. Typical SRS images of the tissues. B. SRS spectra. C. SRS images taken at CH2 (2845 cm-1) and CH3 (2930 cm-1) channels of the nerve root, and the decomposed distributions of lipid (green) and protein (blue). D. SRS intensity profiles along the yellow dashed line. E. Normalized SRS spectra of the three selected regions shown in Fig. 2(D). Scale bar: 25 μm.

characteristics more akin to lipids, whereas IVD and LF shared similar SRS profiles to protein [32].

To further reveal the structural and biochemical characteristics of nerve roots, different regions from inside to outside of the nerve root (nerve, dura and the border between them) were analyzed. SRS images taken at the two typical Raman frequencies, CH2 (2845 cm-1) and CH3 (2930 cm-1) are shown in Fig. 2(C). Based on the SRS spectra of standard pure chemicals [32], lipids are known to yield high signal intensity at both 2845 cm-1 and 2930 cm-1, whereas proteins generate high signal at 2930 cm-1 but low intensity at 2845 cm-1. It is thus clearly seen that the myelinated nerves contain high lipid level, while the dura is mainly consisted of protein rich content. After numerical decomposition of the two SRS raw images into the distribution of lipids (green) and proteins (blue) [25,32], nerve structures and peripheral dura could be readily distinguished (Fig. 2(C)).

The intensity profiles of SRS signal across the interface of nerve/dura along the yellow dashed line in Fig. 2(C) are shown in Fig. 2(D). As can be seen, lipids appear relatively even distribution from the inside to the outside of the nerve root, while proteins demonstrated an increasing trend in the same direction because of the appearance of the dura tissues. Normalized SRS spectra further confirmed the chemical compositions of different regions of interest, including the nerve (region 1), dura (region 2) and their mixtures (region 3). As shown in Fig. 2(E), region 1 presented lipid spectral signatures, regions 2 presented protein spectrum, and region 3 generated the mixture of lipid and protein profiles. In addition, SRS spectra in region 3 was found to be well fitted by the linear combination of those in regions 1 and 2, demonstrating the overlap of nerve and gristle in region 3, which also reflected the difficulty of nerve protection during surgery.
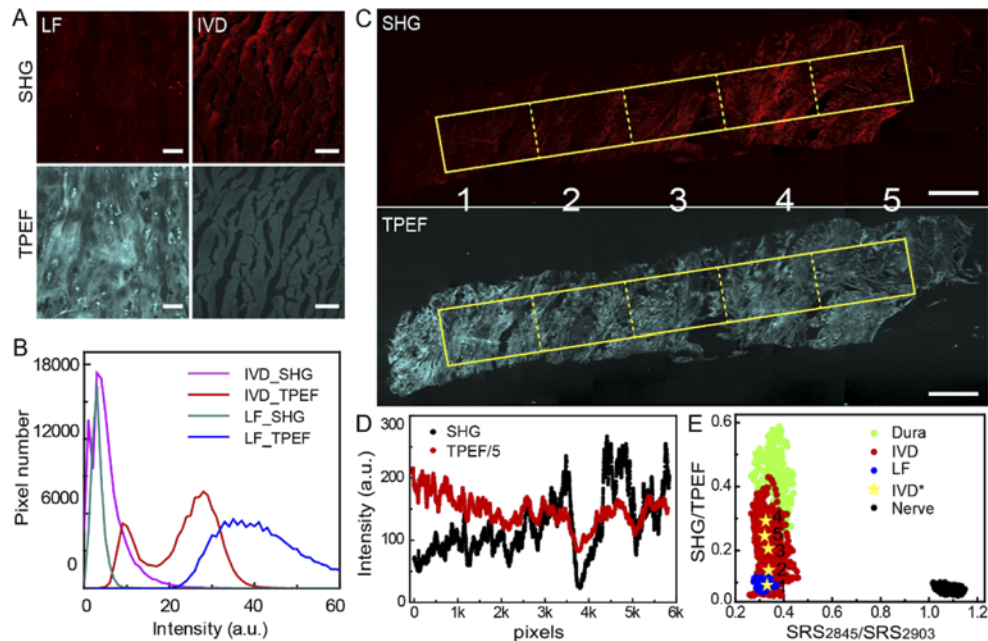

Fig. 3. Characterizing the IVD and LF with SHG and TPEF. A. SHG and TPEF images of the IVD and the LF. B. The corresponding intensity distributions showed. C. An IVD tissue with ordered regions 1-5 from the inner to the outer layer. D. Intensity distribution of SHG and TPEF signal along the direction of the box in C. E. Differentiation of the tissues with combined SHG/TPEF ratio and SRS2845/SRS2930 ratio. Asterisk points represent averaged ratio of the numbered regions in C. Scale bars: 25 μm for A, 500 μm for C.

3.2.   Differentiating IVD and LF with SHG/TPEF

Now that the nerves have been shown to be well identified by SRS, but IVD and LF did not show significant Raman spectral differences for direct differentiation. We next evaluated the possibility of distinguishing IVD and LF with other means of nonlinear optical imaging methods. Luckily, SHG and TPEF imaging results indicated that the IVD contained both high levels of collagen (SHG) and elastic fibers (TPEF). In contrast, LF showed rich elastic fibers but rarely any collagen fibers, as shown in Fig. 3(A). The corresponding intensity distributions also confirmed that the IVD had overall stronger SHG but weaker TPEF signal than LF (Fig. 3(B)), which provide the basis for the differentiation of IVD and LF.

To reveal the spatial heterogeneity of the IVD tissues based on SHG and TPEF imaging, a region from the inner to the outer layers of the IVD was selected for further analysis (Fig. 3(C)). The inner layer of the IVD demonstrated weaker SHG intensity than the outer layer, which indicated that the interior of the IVD contained less collagen fibers. In contrast, the distribution of elastic fibers in the IVD tissue appeared relatively even as seen in the TPEF distribution. These
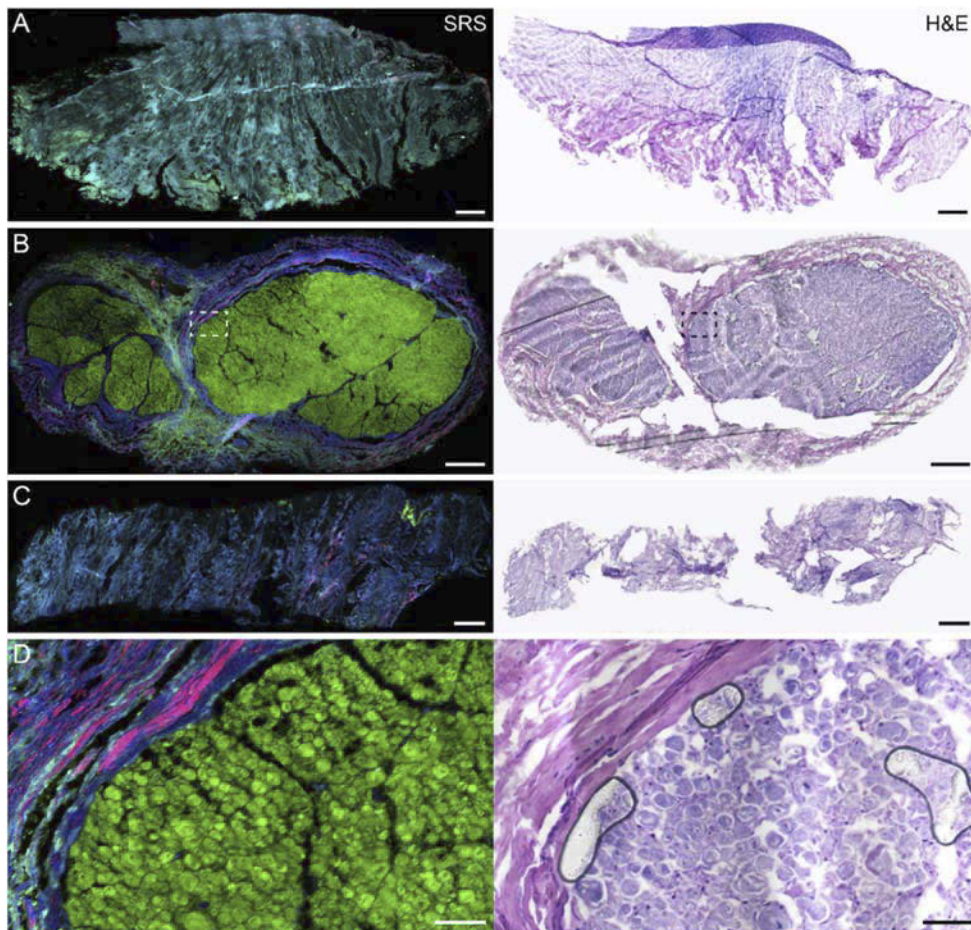

Fig. 4. H&E staining and corresponding nonlinear optical images of different types of tissues. A. LF tissue. B. The dura mater and nerve root. C. IVD tissue (Left: inner part; right: outer part). D. Magnified view of the dashed area in B. Cyan: elastic fibers; Red: collagen fibers; Green: lipids; Blue: protein. Scale bar: 200 μm in A-C, 20 μm in D.

distribution differences could also be confirmed by the intensity profiles along the directions of the rectangular boxes (Fig. 3(D)).

At last, in order to effectively differentiate the three key structures (nerve root, IVD and LF) we need to fully use the integrated information of SRS, SHG and TPEF. First of all, the nerve root could be well separated by the ratio of SRS signal at the two Raman frequencies (SRS2845/SRS2930), which reflects the relative lipid content (higher lipid corresponds to higher ratio). Therefore, the SRS2845/SRS2930 ratio was set as the horizontal axis (Fig. 3(E)). Then, to further differentiate IVD and LF, the ratio of collagen to elastic fiber (SHG/TPEF) was set as the vertical axis (Fig. 3(E)), showing separated clusters of LF from IVD. Note the SHG/TPEF ratio in IVD appears more diverse and spread due to the heterogeneous distribution of collagen fibers (Fig. 3(C)).

3.3. Multi-model imaging of dura mater, IVD and LF tissues

H&E staining and the corresponding multi-modal multiphoton imaging results are shown in Fig. 4. Multiphoton imaging not only showed tissue morphology similar to H&E staining, but also provided chemical distributions for the specific identification. In a typical LF tissue, regularly arranged fibers could be revealed by both H&E and multiphoton imaging. However, multiphoton image indicated additional information of rich elastic fibers but rare collagen fibers in LF (Fig. 4(A)). In a cross-section tissue of dura mater, the lipid rich nerves could be readily visualized by SRS, and the surrounding dura mater could also be seen as regularly arranged collagen and elastic fibers (Fig. 4(B)). And the IVD tissue showed more elastic fibers in the inner part and more collagen fibers in the outer part (Fig. 4(C)). High-resolution, magnified views of the nerve/dura interface clearly differentiated the fibers and myeline (Fig. 4(D)).

4. Discussion

During PELD, fibrotic adhesion can be observed between the dura (nerve root) and the surrounding structures, particularly due to their similar visual appearances to the naked eye, therefore, it is necessary to clearly distinguish between them. The multiphoton imaging features of the lumbar spine structures were shown in our study for the first time. Additionally, our study found that nonlinear optical microscopic appearances of the dura and the adjacent soft tissues differed significantly. Although the current work has been focused on thin tissue sections, the method could be easily adapted to fresh tissues and even in vivo studies, which holds great potentials for intraoperative identification of different types of peridura tissues during PELD.

The IVD is the joint of the spine [38] and consists of the NP in the center, surrounded by the AF laterally and by the cartilaginous endplates vertically. Type I and II collagens are the main components of AF and form concentric lamellae around the NP [39]. The AF can be separated into the inner AF and the outer AF. The outer AF consists of an oriented lamellar collection of densely packed collagen fibers, whereas the inner AF is identical to the external parts except that it is not as thick and the directed lamellae are not as regularly arranged [40]. In our study, we found a higher SHG signal in the outer AF and a relatively lower SHG signal in the inner AF, and these findings confirm the aforementioned molecular biology findings. In this study, rather than to differentiate collagen types, multiphoton technique provided a rapid and nontoxic method to identify tissues with different collagen content, which will be very useful for the rapid identification of different tissues during surgery.

Another structural protein found in the IVD is elastin [41], which is present in proportionately small amounts but still can play a significant mechanical role [42,43]. Elastin is the major structural component of most elastic fibers in human tissues, such as the artery wall, lung, ligament, and skin, which require durability for their biological functions [44]. In the study by Yu et al. in Ref. 35, a long elastic fiber aligned with collagen bundles within lamellae and a dense elastic fiber network were visible in the gap between adjacent lamellae in the outer AF

[45]. The elastic fibers in the inner AF were dense and were in an intricate type between adjacent lamellae; the fibers were also very apparent and parallel to each other within individual lamellae [45]. In our study, we found high TPEF signals in both the inner and outer AF, meaning that TPEF was able to sensitively detect the elastic fibers, even though it is only a minor component in the annulus. In addition, an increasing TPEF signal was seen in the disc from the outer to the inner AF, which could be due to the higher density of elastic fibers in the inner AF compared with the outer AF.

The LF surrounds the posterior and lateral walls of the spinal canal. As the LF thickens, it compresses the nerve roots of the cauda equina [46]. Removal of the LF is another major target in PELD due to the thickening of the ligament. Previous studies have shown a reduction of elastic fibers and an increase of collagen fibers in hypertrophied LF [14–16,47]. In addition, synthesis of collagen fibers and degradation of elastic and collagen fibers are both accelerated in the hypertrophied LF [48,49]. After analysis, we found that collagen protein could be clearly identified in LF by SRS microscopy, and its spectral profile was similar to that of AF. Secondly, regarding SHG and TPEF signals, elastic fibers had a stronger presence than collagen fibers in LF. This was mainly due to the tissue being obtained from cadavers at a young age without hypertrophy in LF. Future studies shall include elderly patients.

The dura mater ranges from the foramen magnum to the sacrum and coccyx. Dura extensions cover the nerve roots and go beyond between the IVD and LF. The nerve roots are compressed by herniated discs and hypertrophied LF in lumbar degenerative diseases, and inflammation contributes to adhesions of soft tissues. Hence, the key to improve operational safety is to distinguish the dura mater from the IVD and the LF [8,9]. According to the content and distribution characteristics of elastic fibers and collagen fibers by multi-modal imaging, the dura mater, the IVD and the LF could be easily distinguished. The dural material was rich in both collagen fibers and elastic fibers, and the fibers were regularly aligned. The nerve root inside the dura mater was rich in lipids. The LF was rich in elastic fibers and less abundant in collagen fibers, with regularly aligned dense fiber morphologies. In the IVD, there were more elastic fibers in the inner AF and more collagen fibers in the outer part, the fibers were looser, and the alignment was less regular than that in the dura mater and LF. These distinct compositional and histological features of lumbar spine associated structures will be of great help in identifying different tissues during surgery.

In addition to the discoveries found in this study, several factors will need further developments for the practical application of nonlinear optical microscopy to assist PELD surgery. First of all, although our current study focused on thin tissue sections to reveal the optical properties of lumbar tissues in the transmission mode, epi-detection of thick fresh tissues or *in vivo* imaging will result in weaker signal intensity with preserved optical characteristics [21,24,25]. It is crucial to integrate the nonlinear optical microscopy with endoscopy to fit the surgical setting, which becomes possible with the recent technical advances of coherent Raman endoscopy [50]. Secondly, with the help of deep-learning algorithms, intelligent and automated diagnosis of the nonlinear optical images has shown promise in rapid intraoperative histopathology [22,32]. Both the system development and machine learning are among our on-going research plans along the line.

5. Conclusion

To summarize, our study has revealed the multi-modal nonlinear optical features of lumbar spine associated structures. The nonlinear optical characteristics of different types of peridural soft tissues were significantly different, which provides potentials to differentiate them effectively during PELD surgeries.

Appendix: abbreviations

IVD	intervertebral disc
PELD	percutaneous endoscopic lumbar discectomy
NP	nucleus pulposus
AF	anulus fibrosus
LF	ligamentum flavum
SRS	stimulated Raman scattering
PBS	phosphate-buffered saline
fs	femtosecond
OPO	optical parametric oscillator
ps	picoseconds
SRL	stimulated Raman loss
SHG	second harmonic generation
TPEF	two-photon excitation fluorescence
PMT	photomultiplier
FOV	field of view

Disclosures. The authors declare no conflicts of interest.

Data availability. The data that support the findings of this study are available from the corresponding author upon reasonable request.

References

1. J. Jordan, K. Konstantinou, and J. O'Dowd, "Herniated lumbar disc," in BMJ Clin Evid (2009).
2. F. Postacchini, "Management of herniation of the lumbar disc," J Bone Joint Surg Br **81-B**(4), 567–576 (1999).
3. S. S. Ahn, S. H. Kim, D. W. Kim, and B. H. Lee, "Comparison of outcomes of percutaneous endoscopic lumbar discectomy and open lumbar microdiscectomy for young adults: a retrospective matched cohort study," World Neurosurg **86**, 250–258 (2016).
4. O. O. Akinduro, P. Kerezoudis, M. A. Alvi, J. W. Yoon, J. Eluchie, M. H. Murad, Z. Wang, S. G. Chen, and M. Bydon, "Open versus minimally invasive surgery for extraforaminal lumbar disk herniation: a systematic review and meta-analysis," World Neurosurg **108**, 924–938.e3 (2017).
5. C. W. B. Peng, W. Yeo, and S. B. Tan, "Percutaneous endoscopic discectomy clinical results and how it affects the quality of life," J Spinal Disord Tech **23**(6), 425–430 (2010).
6. S. J. Kamper, R. W. J. G. Ostelo, S. M. Rubinstein, J. M. Nellensteijn, W. C. Peul, M. P. Arts, and M. W. van Tulder, "Minimally invasive surgery for lumbar disc herniation: a systematic review and meta-analysis," Eur Spine J **23**, 1021–1043 (2014).
7. K. Phan, J. Xu, K. Schultz, M. A. Alvi, V. M. Lu, P. Kerezoudis, P. R. Maloney, M. E. Murphy, R. J. Mobbs, and M. Bydon, "Full-endoscopic versus micro-endoscopic and open discectomy: a systematic review and meta-analysis of outcomes and complications," Clin Neurol Neurosur **154**, 1–12 (2017).
8. J. Yokosuka, Y. Oshima, T. Kaneko, Y. Takano, H. Inanami, and H. Koga, "Advantages and disadvantages of posterolateral approach for percutaneous endoscopic lumbar discectomy," J. Spine Surg **2**(3), 158–166 (2016).
9. H. G. Lee, M. S. Kang, S. Y. Kim, K. C. Cho, Y. C. Na, J. M. Cho, and B. H. Jin, "Dural injury in unilateral biportal endoscopic spinal surgery," Glob Spine J **11**(6), 845–851 (2021).

10. S. J. Bosacco, M. J. Gardner, and J. T. Guille, "Evaluation and treatment of dural tears in lumbar spine surgery - a review," Clin Orthop Relat R **389**, 238–247 (2001).
11. M. Protasoni, S. Sangiorgi, A. Cividini, G. T. Culuvaris, G. Tomei, C. Dell'Orbo, M. Raspanti, S. Balbi, and M. Reguzzoni, "The collagenic architecture of human dura mater," J Neurosurg **114**(6), 1723–1730 (2011).
12. M. K. Chelberg, G. M. Banks, D. F. Geiger, and T. R. Oegema, "Identification of heterogeneous cell-populations in normal human intervertebral disc," J Anat **186**, 43–53 (1995).
13. S. Roberts, H. Evans, J. Trivedi, and J. Menage, "Histology and pathology of the human intervertebral disc," J Bone Joint Surg Am **88a**, 10–14 (2006).
14. T. Nakatani, T. Marui, T. Hitora, M. Doita, K. Nishida, and M. Kurosaka, "Mechanical stretching force promotes collagen synthesis by cultured cells from human ligamentum flavum via transforming growth factor-beta1," J. Orthop. Res. **20**(6), 1380–1386 (2002).
15. H. Kosaka, K. Sairyo, A. Biyani, D. Leaman, R. Yeasting, K. Higashino, T. Sakai, S. Katoh, T. Sano, V. K. Goel, and N. Yasui, "Pathomechanism of loss of elasticity and hypertrophy of lumbar ligamentum flavum in elderly patients with lumbar spinal canal stenosis," Spine **32**(25), 2805–2811 (2007).
16. J. B. Park, J. K. Lee, S. J. Park, and K. D. Riew, "Hypertrophy of ligamentum flavum in lumbar spinal stenosis associated with increased proteinase inhibitor concentration," J Bone Joint Surg Am **87**(12), 2750–2757 (2005).
17. M. Yoshida, K. Shima, Y. Taniguchi, T. Tamaki, and T. Tanaka, "Hypertrophied ligamentum flavum in lumbar spinal canal stenosis. Pathogenesis and morphologic and immunohistochemical observation," Spine **17**(11), 1353–1360 (1992).
18. C. Krafft, M. Schmitt, I. W. Schie, D. Cialla-May, C. Matthaus, T. Bocklitz, and J. Popp, "Label-free molecular imaging of biological cells and tissues by linear and nonlinear raman spectroscopic approaches," Angew. Chem. Int. Ed. **56**(16), 4392–4430 (2017).
19. W. Querido, S. Kandel, and N. Pleshko, "Applications of vibrational spectroscopy for analysis of connective tissues," Molecules **26**(4), 922 (2021).
20. J. J. A. Poole and L. B. Mostaco-Guidolin, "Optical microscopy and the extracellular matrix structure: a review," Cells-Basel **10**(7), 1760 (2021).
21. B. G. Saar, C. W. Freudiger, J. Reichman, C. M. Stanley, G. R. Holtom, and X. S. Xie, "Video-rate molecular imaging in vivo with stimulated Raman scattering," Science **330**(6009), 1368–1370 (2010).
22. T. C. Hollon, B. Pandian, A. R. Adapa, E. Urias, A. V. Save, S. S. S. Khalsa, D. G. Eichberg, R. S. D'Amico, Z. U. Farooq, S. Lewis, P. D. Petridis, T. Marie, A. H. Shah, H. J. L. Garton, C. O. Maher, J. A. Heth, E. L. McKean, S. E. Sullivan, S. L. Hervey-Jumper, P. G. Patil, B. G. Thompson, O. Sagher, G. M. McKhann, R. J. Komotar, M. E. Ivan, M. Snuderl, M. L. Otten, T. D. Johnson, M. B. Sisti, J. N. Bruce, K. M. Muraszko, J. Trautman, C. W. Freudiger, P. Canoll, H. Lee, S. Camelo-Piragua, and D. A. Orringer, "Near real-time intraoperative brain tumor diagnosis using stimulated Raman histology and deep neural networks," Nat Med **26**(1), 52–58 (2020).
23. C. W. Freudiger, W. Min, B. G. Saar, S. Lu, G. R. Holtom, C. W. He, J. C. Tsai, J. X. Kang, and X. S. Xie, "Label-free biomedical imaging with high sensitivity by stimulated Raman scattering microscopy," Science **322**(5909), 1857–1861 (2008).
24. R. He, Y. Xu, L. Zhang, S. Ma, X. Wang, D. Ye, and M. Ji, "Dual-phase stimulated Raman scattering microscopy for real-time two-color imaging," Optica **4**(1), 44–47 (2017).
25. M. B. Ji, D. A. Orringer, C. W. Freudiger, S. Ramkissoon, X. H. Liu, D. Lau, A. J. Golby, I. Norton, M. Hayashi, N. Y. R. Agar, G. S. Young, C. Spino, S. Santagata, S. Camelo-Piragua, K. L. Ligon, O. Sagher, and X. S. Xie, "Rapid, label-free detection of brain tumors with stimulated Raman scattering microscopy," Sci. Transl. Med. **5**(201), 201ra119 (2013).
26. M. Ji, S. Lewis, S. Camelo-Piragua, S. H. Ramkissoon, M. Snuderl, S. Venneti, A. Fisher-Hubbard, M. Garrard, D. Fu, A. C. Wang, J. A. Heth, C. O. Maher, N. Sanai, T. D. Johnson, C. W. Freudiger, O. Sagher, X. S. Xie, and D. A. Orringer, "Detection of human brain tumor infiltration with quantitative stimulated Raman scattering microscopy," Sci. Transl. Med. **7**, 309ra163 (2015).
27. L. Zeldin, G. E. Mosley, D. Laudier, Z. S. Gallate, J. Gansau, R. C. Hoy, J. Poeran, and J. C. Iatridis, "Spatial mapping of collagen content and structure in human intervertebral disk degeneration," JOR Spine **3**(4), e1129 (2020).
28. X. Y. Chen, O. Nadiarynkh, S. Plotnikov, and P. J. Campagnola, "Second harmonic generation microscopy for quantitative analysis of collagen fibrillar structure," Nat Protoc **7**(4), 654–669 (2012).
29. E. V. Gubarkova, V. V. Elagin, V. V. Dudenkova, S. S. Kuznetsov, M. M. Karabut, A. L. Potapov, D. A. Vorontsov, A. Y. Vorontsov, M. A. Sirotkina, E. V. Zagaynova, and N. D. Gladkova, "Multiphoton tomography in differentiation of morphological and molecular subtypes of breast cancer: A quantitative analysis," J Biophotonics **14**(5), e202000471 (2021).
30. G. Chen, J. Chen, S. Zhuo, S. Xiong, H. Zeng, X. Jiang, R. Chen, and S. Xie, "Nonlinear spectral imaging of human hypertrophic scar based on two-photon excited fluorescence and second-harmonic generation," Brit J Dermatol **161**(1), 48–55 (2009).
31. T. Meyer, M. Chemnitz, M. Baumgartl, T. Gottschall, T. Pascher, C. Matthaus, B. F. M. Romeike, B. R. Brehm, J. Limpert, A. Tunnermann, M. Schmitt, B. Dietzek, and J. Popp, "Expanding multimodal microscopy by high spectral resolution coherent anti-Stokes Raman scattering imaging for clinical disease diagnostics," Anal. Chem. **85**(14), 6703–6715 (2013).

32. L. L. Zhang, Y. Z. Wu, B. Zheng, L. Z. Su, Y. Chen, S. Ma, Q. Q. Hu, X. Zou, L. Yao, Y. L. Yang, L. Chen, Y. Mao, Y. Chen, and M. B. Ji, "Rapid histology of laryngeal squamous cell carcinoma with deep-learning based stimulated Raman scattering microscopy," Theranostics **9**(9), 2541–2554 (2019).

33. T. Hellerer, A. M. K. Enejder, and A. Zumbusch, "Spectral focusing: high spectral resolution spectroscopy with broad-bandwidth laser pulses," Appl. Phys. Lett. **85**(1), 25–27 (2004).

34. D. Fu, G. Holtom, C. Freudiger, X. Zhang, and X. S. Xie, "Hyperspectral Imaging with stimulated Raman scattering by chirped femtosecond lasers," J. Phys. Chem. B **117**(16), 4634–4640 (2013).

35. L. L. Zhang, S. D. Shen, Z. Liu, and M. B. Ji, "Label-free, quantitative imaging of MoS2-nanosheets in live cells with simultaneous stimulated Raman scattering and transient absorption microscopy," Adv. Biosys. **1**(4), 1700013 (2017).

36. J. P. Ao, X. F. Fang, X. C. Miao, J. W. Ling, H. Kang, S. Park, C. F. Wu, and M. B. Ji, "Switchable stimulated Raman scattering microscopy with photochromic vibrational probes," Nat Commun **12**(1), 3089 (2021).

37. B. H. Zhang, H. L. Xu, J. Chen, X. X. Zhu, Y. Xue, Y. F. Yang, J. P. Ao, Y. H. Hua, and M. B. Ji, "Highly specific and label-free histological identification of microcrystals in fresh human gout tissues with stimulated Raman scattering," Theranostics **11**(7), 3074–3088 (2021).

38. S. Roberts, J. P. Urban, H. Evans, and S. M. Eisenstein, "Transport properties of the human cartilage endplate in relation to its composition and calcification," Spine **21**(4), 415–420 (1996).

39. D. R. Eyre and H. Muir, "Quantitative analysis of types I and II collagens in human intervertebral discs at various ages," Biochimica et Biophysica Acta (BBA) - Protein Structure **492**(1), 29–42 (1977).

40. B. R. Whatley and X. J. Wen, "Intervertebral disc (IVD): Structure, degeneration, repair and regeneration," Mat Sci Eng C-Mater **32**(2), 61–77 (2012).

41. Y. Mikawa, H. Hamagami, J. Shikata, and T. Yamamuro, "Elastin in the human intervertebral-disk - a histological and biochemical-study comparing it with elastin in the human yellow ligament," Arch Orthop Traum Su **105**(6), 343–349 (1986).

42. K. Olczyk, "Age-related-changes of elastin content in human intervertebral disks," Folia Histochem Cyto **32**, 41–44 (1994).

43. J. Yu, C. Peter, S. Roberts, and J. P. G. Urban, "Elastic fibre organization in the intervertebral discs of the bovine tail," J Anat **201**(6), 465–475 (2002).

44. E. G. Cleary and M. A. Gibson, "Elastin-associated microfibrils and microfibrillar proteins," Int Rev Connect Tiss **10**, 97–209 (1983).

45. J. Yu, J. C. T. Fairbank, S. Roberts, and J. P. G. Urban, "The elastic fiber network of the anulus fibrosus of the normal and scoliotic human intervertebral disc," Spine **30**(16), 1815–1820 (2005).

46. K. Sairyo, A. Biyani, V. Goel, D. Leaman, R. Booth, J. Thomas, D. Gehling, L. Vishnubhotla, R. Long, and N. Ebraheim, "Pathomechanism of ligamentum flavum hypertrophy: a multidisciplinary investigation based on clinical, biomechanical, histologic, and biologic assessments," Spine **30**(23), 2649–2656 (2005).

47. K. Zhang, W. Sun, X. Y. Liu, C. Q. Zhao, H. Li, X. J. Sun, Y. Z. Xie, W. Ding, and J. Zhao, "Hypertrophy and fibrosis of the ligamentum flavum in lumbar spinal stenosis is associated with increased expression of LPA and LPAR1," Clin Spine Surg **30**(3), E189–E191 (2017).

48. Y. Yabe, Y. Hagiwara, A. Ando, M. Tsuchiya, T. Minowa, T. Takemura, M. Honda, K. Hatori, K. Sonofuchi, K. Kanazawa, M. Koide, T. Sekiguchi, and E. Itoi, "Chondrogenic and fibrotic process in the ligamentum flavum of patients with lumbar spinal canal stenosis," Spine **40**(7), 429–435 (2015).

49. Y. Yabe, Y. Hagiwara, M. Tsuchiya, M. Honda, K. Hatori, K. Sonofuchi, K. Kanazawa, M. Koide, T. Sekiguchi, N. Itaya, and E. Itoi, "Decreased elastic fibers and increased proteoglycans in the ligamentum flavum of patients with lumbar spinal canal stenosis," J. Orthop. Res. **34**(7), 1241–1247 (2016).

50. A. Lombardini, V. Mytskaniuk, S. Sivankutty, E. R. Andresen, X. Chen, J. Wenger, M. Fabert, N. Joly, F. Louradour, A. Kudlinski, and H. Rigneault, "High-resolution multimodal flexible coherent Raman endoscope," Light Sci Appl **7**(1), 10 (2018).